# Quantification of Cervical Elasticity During Pregnancy Based on Transvaginal Ultrasound Imaging and Stress Measurement

Peng Hu ⊕, Peinan Zhao ⊕, Yuan Qu ⊕, Konstantin Maslov ⊕, Jessica Chubiz, Methodius G. Tuuli, Molly J. Stout ⊕, and Lihong V. Wang ⊕, *Fellow, IEEE*

*Abstract*—Strain elastography and shear wave elastography are commonly used to quantify cervical elasticity. However, the absence of stress information in strain elastography causes difficulty in inter-session elasticity comparison, and the robustness of shear wave elastography is compromised by cervical tissue's high inhomogeneity. *Objective:* To overcome these limitations, we develop a quantitative cervical elastography system by adding a stress sensor to a clinically used transvaginal ultrasound imaging system. *Methods:* We record the cervical deformation in B-mode images and measure the probe-surface stress through the sensor. Then we quantify the strain using a customized algorithm and estimate the cervical Young's modulus through stress-strain linear regression. *Results:* In phantom experiments, we demonstrate the system's high accuracy (alignment with the quasi-static compression method, *p*-value = 0.369 > 0.05), robustness (alignment between 60°- and 90°-contact measurements, *p*-value = 0.638 > 0.05), repeatability (consistency of single sonographers' measurements, coefficient of variation < 0.06), and reproducibility (alignment between two sonographers' measurements, Pearson correlation coefficient = 0.981). Applying it to pregnant participants, we observe significant cervical softening (*p*-value < 0.001): Young's modulus decreases 3.95% weekly and its geometric mean value during the first (11 to 13 weeks), second, and third trimesters are 13.07 kPa, 7.59 kPa, and 4.40 kPa, respectively. *Conclusion:* The proposed system is accurate, robust, and safe, and enables longitudinal and inter-examiner comparisons. *Significance:* The system applies to different ultrasound machines with minor software updates, which allows for studies of cervical softening patterns in pregnancy for larger populations, facilitating insights into conditions such as preterm birth.

*Index Terms*—Feature tracking, quantitative cervical elastography, stress measurement, strain quantification, transvaginal ultrasound imaging, young's modulus.

## I. INTRODUCTION

PRETERM birth (delivery < 37 weeks of gestation) is the most significant cause of neonatal morbidity and mortality [1]. Due to the high risks of prematurity to a neonate, maternal hospitalization in patients with preterm labor symptoms accounts for 1/3 of antepartum hospitalizations. Yet, more than half of women hospitalized with threatened preterm labor go on to deliver at term [2]. For better management, there is a demanding need to develop tools to predict premature delivery more accurately.

Cervical ripening is the process by which the cervix undergoes changes to soften, shorten, and dilate to allow passage of the fetus in delivery. Although manual palpation (Bishop score) has been used to estimate cervical softening, its predictive utility for preterm birth is limited [3]. A quantitative method to document cervical softening before detectable dilation could significantly advance the field of preterm birth prediction.

Ultrasound elastography is commonly used to quantify tissue elasticity due to its wide availability and relatively low cost [4]. It includes stress-strain elastography and shear wave elastography [4], [5], [6], [7], [8], [9], [10], [11], which measure tissue Young's modulus and shear wave speed, respectively. In clinical practice, stress-strain elastography is simplified to strain elastography [4], [6], [7], [10], [11] and has been widely applied to the breast, prostate, liver, and thyroid where regional tissue-elasticity differences are clinically useful [12], [13], [14], [15], [16], [17]. However, without stress information, strain elastography does not support comparisons between different imaging sessions.

Shear wave elastography [4], [5], [8], [9] is also used clinically to measure shear wave speed in the breast [5], [18], [19], [20], prostate [5], [21], [22], liver [23], [24], [25], [26], [27],

and thyroid [28], [29], [30], and the measurement allows for longitudinal analysis. Although it has been applied to the cervix [31], [32], [33], [34], [35], [36], [37], [38], [39], there are some limitations. First, the homogeneous-tissue assumption for shear wave elastography is violated in the cervix by cystic areas, blood vessels, endocervical canal, and layers of collagen with varying alignments [38], [40]. Second, tissue excitation changes that shear waves potentially elicit [41], [42] make shear-wave-free ultrasound elastography safer during pregnancy. Third, operator and patient-dependent factors [38], [43], [44], such as the stress applied to the cervix, may affect the shear wave speed.

Thus, to optimize the characterization of normal and abnormal cervical ripening, a quantitative system is required that is operator-independent and can provide reliable measurements in the same patient over time and for between-patient comparisons. To address the limitations in existing systems described above and to meet the required characteristics for quantification of cervical ripening, we describe herein the development of a protocol based on transvaginal ultrasound that is safe in pregnancy, operator-independent, and quantitative, using stress-strain elastography to capture cervical tissue elasticity. We develop the system by adding a stress sensor to a clinically used transvaginal ultrasound imaging system; demonstrate its high accuracy, low contact-angle dependency, high repeatability, and high reproducibility in phantom experiments; and validate its effectiveness in monitoring cervix softening by applying it to pregnant participants.

## II. METHODS

### A. Quantitative Cervical Elastography System

The quantitative cervical elastography system, as summarized in Fig. 1(a), is based on three components: a transvaginal ultrasound imaging system, a stress measurement system, and a stress calibration system. Two transvaginal B-mode images of a cervix (posterior boundary marked as a red-dashed curve) are shown in Fig. 1(b1) and (b2), respectively, from which the cervix deformation is observed. A series of quantified strains are shown in Fig. 1(c). The stress measurement system is visualized in Fig. 1(d1) and (d2) and a series of measured stresses are plotted in Fig. 1(e). The calibration system is depicted in Fig. 1(f1) and (f2) with a calibration function shown in Fig. 1(g), which inversely transforms the stress measurements to true stresses (Fig. 1(h)) and allows for the final linear regression shown in Fig. 1(i). To facilitate the operation, we developed a graphical user interface (GUI) for participant imaging (Supplementary Note 1).

### B. Strain Quantification

Radiofrequency (RF) signals are preferred for strain quantification in ultrasound imaging but are usually inaccessible in clinically used ultrasound machines. In this study, we propose an algorithm to quantify cervical strain from all the frames in each B-mode video and we analyze the strain only along the ultrasound probe axis. First, we quantify the cervical deformation between every pair of consecutive frames in the video through
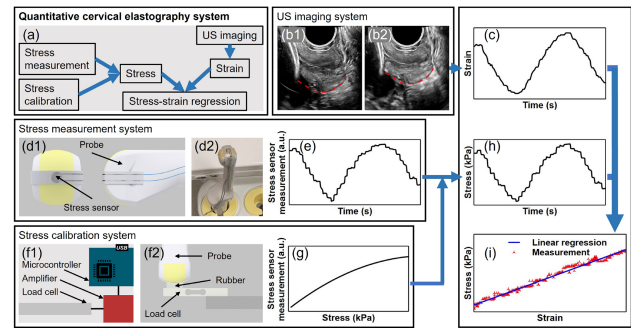


Fig. 1. Quantitative cervical elastography system. (a) The general workflow of the quantitative cervical elastography system. (b1)–(b2) Two B-mode images of a cervix (posterior boundary marked as a red-dashed curve), showing deformation of the cervix. (c) Strains of the cervix quantified from the continuously acquired B-mode images. (d1)–(d2) A stress sensor embedded into a layer of silicone sealant and mounted to the probe. (e) A series of measured stresses. (f1)–(f2) A stress sensor calibration system, consisting of a load cell, a load cell amplifier, and a microcontroller board. During calibration, a layer of silicone rubber is placed between the probe and the load cell to stabilize contact. (g) A calibration function describing the relation between stress sensor measurement and the true stress. (h) A series of true stresses obtained by calibrating the stress sensor measurements in (e) using the calibration function in (g). (i) A stress-strain scatter plot and its linear regression using the strains in (c) and the stresses in (h).

a correlation-based method and calculate the deformation between two arbitrary frames through recursion (Supplementary Note 2). Next, we correct the accumulative error in the recursion based on the periodicity of the deformation (Supplementary Note 3). Then we quantify the logarithmic strain of the cervical tissue from the cervical deformation (Supplementary Note 4).

### C. Stress Measurement

We customize a stress sensor (FlexiForce A101) and mount it to the ultrasound probe for stress measurement. The currently used stress sensor can be damaged if directly used in an aqueous environment. To make it waterproof, we embed it into a layer of silicone sealant, which also stabilizes the contact for robust measurement. Before each measurement, both the ultrasound probe and stress sensor are disinfected; then they are dried for stable contact. Next, the ultrasound probe is connected to the ultrasound machine, and the two wires soldered to the stress sensor are connected to a microcontroller board. The stress sensor sampling rate is set as 80 Hz, higher than the frame rate (30 Hz) of the B-mode videos from the ultrasound system. Then the stress sensor is mounted onto the tip of the probe and fixed by two rubber bands. After sensor mounting, a syringe is used to inject ultrasound gel into the space between the silicone sealant and the probe. The stress sensor covers a relatively small area of the detection surface of the ultrasound probe. The ultrasound transmits through the silicone sealant in other parts of the detection surface and the ultrasound image is minorly affected by the stress sensor.

### D. Stress Calibration

We designed a calibration system using a load cell, a load cell amplifier, and a microcontroller board and the system is

used to calibrate the stress sensor after each imaging session. The load cell (maximum weight of 780 g) is calibrated with standard weights right after initial setup and in the following weekly maintenance. For stress sensor calibration, to stabilize the contact, a layer of rubber is placed between the load cell and the stress sensor mounted on the probe. Multiple press-release cycles are applied to the probe along its axial direction so that the stress sensor responses cover the whole range of measurements for cervical tissue. Measurements from the stress sensor and load cell during these cycles are used for calibration. For an imaging session, we denote the calibration function as $f_{cal}$, which maps the true stress to the stress sensor measurement (Supplementary Note 5).

### E. Stress-Strain Regression

The measurement from a single stress sensor does not have enough information to determine the stress distribution along the probe axis. In this research, we use the stress sensor measurement to approximate the average stress along the probe axis. We denote the stress sensor measurement corresponding to the $l$-th frame in the B-mode video as $\tilde{\sigma}_l$, which is calibrated to the true stress $f_{cal}^{-1}(\tilde{\sigma}_l)$, and the cervical strain between the first and the $l$-th frame as $\epsilon_l, l = 1, 2, \ldots, L$. Applying a linear regression to the stresses and strains, we obtain

$$f_{cal}^{-1}(\tilde{\sigma}_l) \approx E\epsilon_l + b, l = 1, 2, \ldots, L. \tag{1}$$

Here, $E$ and $b$ denote the estimated Young's modulus and the intercept, respectively.

### F. Pregnant Participant Inclusion

Pregnant participants in this study were from a prospective, longitudinal cohort study [45] performed at Washington University in St. Louis Medical Center between January 2017 and January 2020. These participants were asked to visit from their first trimester to delivery, with gestational ages from 11 to 38 weeks. For this research, we include those (22 participants) with three or more imaging visits that meet the measurement quality requirement for this study and the last visit greater than 34-week gestational age. Characteristics of these participants are shown in Supplementary Table I. Approval of all ethical and experimental procedures and protocols was granted by the Institutional Review Board of Washington University in St. Louis. All participants provided written informed consent for the collection and use of clinical, imaging, and questionnaire data.

### G. Pregnant Participant Cervical Imaging

During a quantitative cervical elastography imaging session, a trained obstetric sonographer obtains a sagittal view of the cervix which shows the cervical stroma and cervical canal using the Hitachi Noblus ultrasound system with a transvaginal ultrasound probe (C41V, 4–8 MHz). The cervix should occupy no less than 2/3 of the imaging depth and be located at the center of the image. Stress is gently applied and released in 2 to 4 cycles (4 seconds) compressing and releasing the tissue

along the probe-axis direction, while the B-mode images are continuously recorded to a video (120 frames, 30-Hz frame rate) and the stress is measured by a stress sensor. At least three videos are acquired for each participant in this research. Stress sensor measurements are calibrated after each imaging session of a participant to obtain true stresses, and strains are quantified from frames in each B-mode video. Linear regression is applied to the stresses and strains to estimate Young's modulus of the cervix. The geometric mean value of multiple estimated Young's moduli in an imaging session of a participant is used to represent the Young's modulus of the session.

### H. Measurement Quality Requirement

During an imaging session, the Pearson correlation coefficient (PCC) between the cervical strains and stress sensor measurements is calculated (denoted as $r'_{ss}$) after each B-mode video is acquired. These videos, cervical strains, stress sensor measurements, and the values of $r'_{ss}$ are used to guide the sonographer to maintain or improve the measurement quality. After an imaging session, we use two parameters to estimate the measurement quality. The PCC between the stress sensor measurements and load cell measurements in a calibration, denoted as $r_{cal}$, is used to estimate sensor performance. To reject errors caused by stress sensor malfunction, we analyze only measurements with $r_{cal} \geq 0.85$. After stress sensor calibration and strain quantification, the PCC between the stresses and strains is calculated, denoted as $r_{ss}$. To reduce errors caused by imperfect operations, only measurements with $r_{ss} \geq 0.8$ are used to estimate Young's moduli. All measurements with $r_{cal} < 0.85$ or $r_{ss} < 0.8$ suggested high noise in the stress or strain measurement and were excluded.

### I. System Accuracy, Repeatability, and Reproducibility

We tested the accuracy, repeatability, and reproducibility of the proposed system in phantom and participant experiments. In the phantom experiments, we prepared four gelatin phantoms with concentrations 70 g/L, 90 g/L, 110 g/L, and 130 g/L, respectively. Two operators used two stress sensor replicas, respectively, to perform the quantitative elastography on each phantom 10 times. One of the operators also used the standard quasi-static compression method to measure the Young's modulus of each phantom 10 times. All measurements from both operators were then compared to evaluate the agreements between the two methods (accuracy), between repetitions (repeatability), and between operators (reproducibility). In the participant experiments, two sonographers performed the quantitative elastography on a pilot cohort of 19 participants. Each participant was measured by two sonographers using the quantitative cervical elastography system at least three times during the visit. The measurements were then compared to evaluate the repeatability and reproducibility of the system.

### J. Statistical Analysis

The PCCs were used to evaluate the linear correlation between the stress sensor measurement and load cell measurement, and that between the strain and true stress. The two-way analysis of
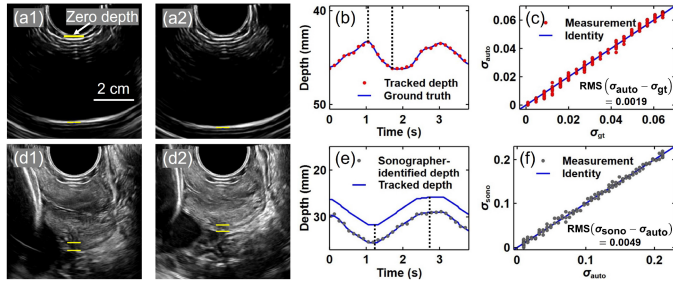
Fig. 2. Correlation-based automatic strain quantification. (a1)–(a2) Two frames in a B-mode video of a gelatin phantom. The lower boundary of the phantom is marked as a yellow bar. (b)–(c) Comparison of ground-truth depths and tracked depths of the lower boundary of the phantom (b) and the quantified strains (c). (d1)–(d2) Two frames in a B-mode video of a cervix. Two features with center depths marked as yellow bars are tracked. (e)–(f) Tracked depths of the two features, sonographer-identified depths of the deeper feature (e), and quantified strains of the deeper feature (f).

variance (ANOVA) [46] was used to test the difference between the proposed method and the standard quasi-static compression method (Supplementary Note 6) in measuring elasticity. The coefficient of variation (CV) was used to quantify the repeatability of multiple measurements performed by an operator (a sonographer) on a phantom (participant). The Bland-Altman plot [47] for the reproducibility test was used to analyze the agreement between sonographers' measurements. The linear mixed model was used to analyze the decreasing trend of Young's moduli during pregnancy. The gestational ages of the measurements were considered as fixed longitudinal effects to Young's moduli. The individual difference was considered as a random intercept/slope effect to describe the inter-patient variability. A test with $p$-value $< 0.05$ was considered statistically significant. All analyses were performed using R statistical software v4.1.2 (R Core Team 2021).

## III. RESULTS

### A. Accuracy of Strain Quantification

Automatization of our quantitative cervical elastography system relies on automatic strain quantification. We demonstrate the accuracy of strain quantification in phantom and participant experiments. In the phantom experiment, we track the thickness of a layer of gelatin phantom while it is vertically pressed by the ultrasound probe. We place a layer of gelatin phantom on a metal plate and use the probe to press the phantom and record the B-mode video. Two frames of the video are shown in Fig. 2(a1) and (a2), respectively. In each frame, the lower boundary of the phantom is marked by a yellow bar. Depths of the lower boundary in different frames are shown in Fig. 2(b), in which, the two black-dotted vertical lines indicate the times of the two frames, respectively, the tracked depths are indicated by red dots, and the direct measurements of the thickness through a linear stage (ground-truth depths) are marked by a blue-solid curve. The root-mean-square (RMS) error between measurements from the two methods is 0.087 mm, which is much smaller than the

deformation amplitude of 2.9 mm (error rate: $0.087/2.9 = 3.0\%$). We further quantify strains $\sigma_{auto}$ and $\sigma_{gt}$ from the automatically tracked depths and the ground-truth depths, respectively. We compare the strains in Fig. 2(c), where the values of ($\sigma_{gt}$, $\sigma_{auto}$) are marked by red dots and the identity relation is indicated by a blue-solid line. The RMS error between $\sigma_{gt}$ and $\sigma_{auto}$ is 0.0019 (3.0% of the amplitude of $\sigma_{gt}$: 0.0642), which shows a high accuracy of the automatic strain quantification algorithm.

Next, we apply this algorithm to a B-mode video of a participant's cervix. Two frames of the video are shown in Fig. 2(d1) and (d2), respectively. Two features (marked as yellow bars) are tracked, and the depths of the two features in different frames are shown in Fig. 2(e), in which, the times of the two frames are indicated by two black-dotted vertical lines, respectively, and the tracked depths of the two features are denoted by two blue-solid curves. For further validation, we let a sonographer identify the depths of the deeper tracked feature (posterior boundary of the cervix) in all the 120 frames, shown as gray dots in Fig. 2(e). We quantify strains $\sigma_{auto}$ and $\sigma_{sono}$ from the automatically tracked depths and sonographer-identified depths, respectively, and plot in Fig. 2(f) the values of ($\sigma_{auto}$, $\sigma_{sono}$) (gray dots) with an identity (blue-solid) line. The RMS error between $\sigma_{auto}$ and $\sigma_{sono}$ (0.0049) is 2.3% of the amplitude of $\sigma_{auto}$ (0.2118), which further demonstrates the high accuracy of the strain quantification algorithm.

### B. Accuracy, Repeatability, and Reproducibility of the System

We demonstrate the accuracy, repeatability, and reproducibility of the quantitative elastography system in phantoms experiments and a pilot study of 19 pregnant participants. We first visualize the measurement quality using a phantom experiment as an example. In Fig. 3(a), the first frame of a B-mode video of a gelatin phantom is shown. The depths of multiple features of the image are marked as white bars. We apply a threshold of one third of the maximum pixel value to all images in the video to reject weak scattering regions. In the remaining regions, using the correlation-based automatic feature tracking algorithm, we obtain the depths of the marked features in different frames. For each tracked feature, the PCC between the tracked depths and the minus stress sensor measurements is further calculated. Depths and PCCs for the tracked features (close to the lower boundary) are shown in Fig. 3(b) and (c), respectively. The zero-depth layer (probe surface) is marked by a red line and a red dot in Fig. 3(b) and (c), respectively; while the tracked features are marked by blue curves and dots, respectively. The mean depth of the tracked features close to the lower boundary is an estimation of the depth of the lower boundary. The depths of the zero-depth layer and the lower boundary are used to calculate the strains, which are in a range from 0 to 0.111 as shown in Fig. 3(d). The stress calibration of this measurement is shown in Fig. 3(e). The stress sensor measurements and true stresses for the calibration are shown as a scatter plot, while the corresponding nonparametric regression [48] is shown as a blue-solid curve ($f_{cal}$). In this experiment, the stress sensor measurements of interest are in a range from 561
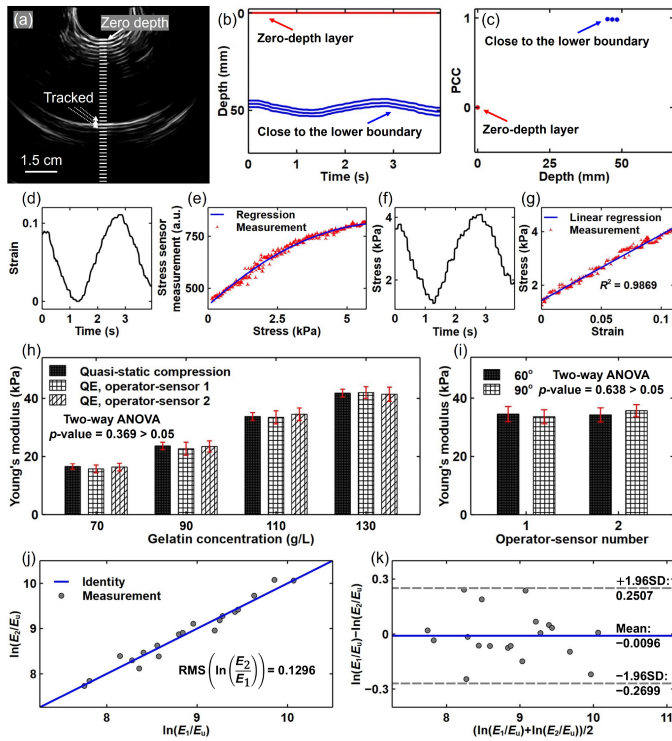
Fig. 3. Accuracy, repeatability, and reproducibility of the quantitative elastography system. (a) The first frame of a B-mode video of a gelatin phantom with depths of multiple features marked as white bars. The three tracked layers (close to the lower boundary) are indicated. (b) Depths tracked by the correlation-based algorithm of the features close to the probe surface or lower boundary of the phantom. (c) PCCs between the tracked depths in (b) and the minus stress sensor measurements. (d) Strains calculated between depths of the zero-depth layer and the lower boundary. (e) Calibration of a stress sensor. The scatter plot represents the calibration measurements, and the blue-solid curve is the nonparametric regression. (f) True stresses in one measurement of the phantom. (g) Scatter plot of the stresses and strains with the linear regression. (h) Comparison of measurements from the quantitative elastography (QE) by two operators using two randomly chosen stress sensor replicas and from the quasi-static compression method for gelatin phantoms of concentrations 70 g/L, 90 g/L, 110 g/L, and 130 g/L, respectively. (i) Measurements of a phantom from QE by two operators using two stress sensors with contact angles of 60° and 90°. (j) Measurements of the 19 participants by two sonographers. Each gray dot of coordinates $(\ln(\frac{E_1}{E_u}), \ln(\frac{E_2}{E_u}))$ represents a participant with measurements $E_1$ and $E_2$ from the two sonographers, respectively. (k) The Bland-Altman plot of the measurements from the two sonographers.

to 760, corresponding to true stresses from 1.25 kPa to 4.06 kPa. In this range of the calibration function $f_{cal}$, the mean difference of the 95% confidence curves (Supplementary Fig.3(c)) is 3.07 (error rate: $3.07/(760 - 561) \approx 1.5\%$), which is negligible for this research. Through calibration, stress sensor measurements for the phantom are transformed into true stresses, as shown in Fig. 3(f). The stresses and strains of this gelatin phantom have a strong linear relation (with $R^2 = 0.9869$), as shown in Fig. 3(g), which agrees with the results in Hall et al. [49]. The slope of this linear model is an estimation of Young's modulus of this phantom.

Next, we apply the proposed quantitative elastography and the standard quasi-static compression method (Supplementary

Fig. 4(a)) to four gelatin phantoms with concentrations of 70 g/L, 90 g/L, 110 g/L, and 130 g/L, respectively. Two randomly chosen stress sensor replicas are used by two operators, respectively, in the quantitative elastography, and each stress sensor is used to measure each phantom 10 times. The quasi-static compression method is also used to measure each phantom 10 times. As shown in Fig. 3(h), the two operators have similar measurements, and the two methods have similar measurements. Statistically, we test the quantitative elastography's dependency on operator-sensor choice and the method's difference from the quasi-static compression method by performing the two-way ANOVA on these measurements. The two-way ANOVA shows no significant differences ($p$-value $= 0.369 > 0.05$) among measurements using the quantitative elastography with operator 1 and stress sensor 1 (operator-sensor 1), the quantitative elastography with operator 2 and stress sensor 2 (operator-sensor 2), and the quasi-static compression method. Here, the operator-sensor difference is considered the random block effect. Moreover, we calculate the CVs of these measurements: 0.0854, 0.0987, 0.0672, and 0.0478 (0.0833, 0.0820, 0.0625, and 0.0586) for the four phantoms, respectively, using the quantitative elastography with operator-sensor 1 (operator-sensor 2); 0.0587, 0.0528, 0.0392, and 0.0318 for the four phantoms, respectively, using the quasi-static compression method. The insignificance of the differences in the two-way ANOVA validates the accuracy and reproducibility of the quantitative elastography system and the low values of CV demonstrate the repeatability.

Furthermore, to test contact angles' effects on measurements, we use two stress sensor replicas to measure a gelatin phantom (with a concentration of 110 g/L) with contact angles of 60° and 90° (Supplementary Fig. 4(b) and (c), respectively). As shown in Fig. 3(i), different stress sensors and different contact angles lead to similar results. Quantitatively, the two-way ANOVA shows no significant difference ($p$-value $= 0.638 > 0.05$) between measurements with contact angles of 60° and 90°. Still, the stress sensor difference here is considered as the random block effect. Based on the test, the proposed system has high robustness with respect to the contact angle, which is important for clinical applications.

Then we test the repeatability and reproducibility of the proposed system in a pilot study of 19 pregnant participants. Two sonographers performed the quantitative elastography at least three times (satisfying the measurement quality requirement) on each participant. The mean CVs of the measurements from the two sonographers are 0.0403 and 0.0540, respectively, showing high repeatability of the system in participant experiments. To simplify the analysis of reproducibility, we denote the geometric means of the two sonographers' measurements of each participant as $E_1$ and $E_2$, respectively. Values of $E_1$ and $E_2$ for the 19 participants are compared in Fig. 3(j): each gray dot of coordinates $(\ln(\frac{E_1}{E_u}), \ln(\frac{E_2}{E_u}))$ represents a participant with measurements $E_1$ and $E_2$ from the two sonographers, respectively. Here, we define $E_u = 1$ Pa. All these gray dots are close to the identity line with an error quantified by the RMS of $\ln(\frac{E_2}{E_u}) - \ln(\frac{E_1}{E_u}) = \ln(\frac{E_2}{E_1})$: 0.1296. This value corresponds to a mean relative difference of $e^{0.1296} - 1 \approx 13.84\%$ between
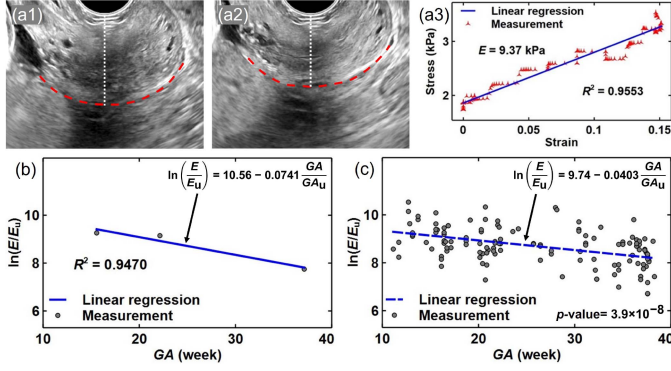
Fig. 4. Longitudinal imaging of pregnant participants. (a1)–(a2) Transvaginal cervical B-mode images (with different stresses) of a participant in one video. The posterior boundary of the cervix is marked by a red-dashed curve. The cervical tissue thickness is indicated by a white-dotted line. (a3) Measured stress-strain values (red three-pointed stars) of this participant in this B-mode video and their linear regression (blue-solid line). A Young's modulus of 9.37 kPa is estimated in the regression. (b) All three measurements (gray dots), expressed as $\ln(\frac{E}{E_u})$, of a participant and their linear regression (blue-solid line). (c) Measurements (gray dots), expressed as $\ln(\frac{E}{E_u})$, of all participants and their linear-mixed-model regression (blue-dashed line).

the two sonographers' measurements $E_1$ and $E_2$. The PCC between $\ln(\frac{E_1}{E_u})$ and $\ln(\frac{E_2}{E_u})$ is 0.981, showing high reproducibility between operators. Furthermore, we compare the measurements in a Bland-Altman plot (Fig. 3(k)), which shows that the measurement differences are within the mean $\pm$ 1.96SD (standard deviation) range and further validates the agreement between the sonographers' measurements.

## C. Longitudinal Imaging of Pregnant Participants

We apply the quantitative cervical elastography system in pregnant participants to quantify cervical Young's moduli longitudinally over pregnancy. The overall success rate of the measurements (the fraction of the measurements that meet the measurement quality requirement) is 54.7%. Performing multiple measurements in every imaging session guarantees a high imaging-session success rate. For example, assuming that different measurements are independent, 3 (4) measurements yield an imaging-session success rate of 90.7% (95.8%). One measurement of a participant is shown in Fig. 4(a1)–(a3). B-mode images of the cervix in the sagittal plane are shown first with minimal stress applied to the tissue (Fig. 4(a1)) where the cervical tissue is noted to be thicker and then as stress is applied (Fig. 4(a2)) the cervical tissue is noted to be thinner. In each image, the posterior boundary of the cervix is marked by a red-dashed curve while the cervical tissue thickness is indicated by a white-dotted line. Strains quantified from the B-mode images are plotted against the measured stresses in Fig. 4(a3) (red three-pointed stars). A linear regression (blue-solid line) is applied to estimate the Young's modulus $E = 9.37$ kPa with $R^2 = 0.9553$.

Quantitative measurement of cervical elasticity allows for the comparison of values from a single participant in different imaging sessions. We analyze three measurements of a participant in three visits, expressed as $\ln(\frac{E}{E_u})$ and denoted by three gray dots, respectively, in Fig. 4(b). Applying linear regression to the three measurements, we obtain $\ln(\frac{E}{E_u}) = 10.56 - 0.0741\frac{GA}{GA_u}$ (with $R^2 = 0.9470$), denoted as a blue-solid line in Fig. 4(b). Here, $GA$ denotes gestational age and we define $GA_u = 1$ week. This linear regression is equivalent to the exponential decaying of shear wave speed during pregnancy [8], [33]. The linear regression result means that the initial cervical Young's modulus of this participant was approximately $e^{10.56}E_u \approx 38.56$kPa. During pregnancy, the cervical Young's modulus of this participant decreased by approximately $1 - e^{-0.0741} \approx 7.14\%$ per week.

Quantitative cervical elastography also allows for the comparison of elasticity among participants. For each participant with three or more visits, we perform linear regression to $\ln(\frac{E}{E_u})$ and obtain $\ln(\frac{E}{E_u}) = \beta_0 - \beta_1\frac{GA}{GA_u}$. The values of $\beta_1$ for these participants have a mean value of 0.0476 with an SD of 0.0302, indicating a general trend of cervical softening and individual variation. Further, we apply a linear-mixed-model regression to $\ln(\frac{E}{E_u})$ of all measurements of these participants and obtain the population average softening trend as $\ln(\frac{E}{E_u}) = 9.74 - 0.0403\frac{GA}{GA_u}$. Values of $\ln(\frac{E}{E_u})$ and the linear regression are shown as gray dots and a blue-dashed line, respectively, in Fig. 4(c). We detect significant softening of the cervix as gestational age increases ($p$-value $< 0.001$). Specifically, we quantify that the geometric mean value of the initial cervical Young's modulus is approximately $e^{9.74}E_u \approx 16.98$kPa, and during pregnancy the cervical Young's modulus decreases by $1 - e^{-0.0403} \approx 3.95\%$ per week. Here, the geometric mean value of Young's modulus $E$ corresponds to the arithmetic mean value of $\ln(\frac{E}{E_u})$. Based on the linear regression, for the first ($11 \leq GA \leq 13$), second ($14 \leq GA \leq 26$), and third ($27 \leq GA \leq 40$) trimesters, the geometric mean values of the cervical Young's moduli are 13.07 kPa, 7.59 kPa, and 4.40 kPa, respectively.

## IV. DISCUSSION

We developed a quantitative cervical elastography system based on transvaginal ultrasound imaging and stress measurement that can be applied to patients during pregnancy to quantify the cervical softening process. Specifically, this system overcomes limitations of prior systems by simultaneously measuring stress and tissue strain, providing a quantitative, operator-independent assessment of cervical tissue elasticity which can be used in the same patient over pregnancy and can be used for between-patient comparisons (development of population norms) as well as within-patient comparisons (identifying patterns of normal or abnormal cervical remodeling in an individual). Importantly, this system is based on minimal modifications to a transvaginal ultrasound probe which is routinely used during pregnancy for other clinical indications and thus is safe, familiar to patients, familiar to healthcare providers, and widely available in obstetric ultrasound units.

The results of the phantom experiments with known elasticities demonstrate accurate and robust agreement among repeated measurements of our system even when the angle of stress application is varied, which addresses the reality of use

*in vivo* where the angle of imaging may vary from patient to patient. Furthermore, the findings from the longitudinal study in pregnant patients demonstrate that the cervix softens over pregnancy, matching the expected pregnancy physiology and previous research.

Technological advancements include the GUI which gives the sonographer real-time information on measurement quality. Additionally, the automatic strain quantification through correlation-based feature tracking enables real-time data analysis and visualization. Although initial stress is still required for good contact, this system captures the stress-strain curve for a large range of stress and applies a linear regression to the curve to estimate Young's modulus, which effectively minimizes the measurement's dependency on initial stress. Importantly, it does not rely on a homogeneous-medium assumption, which is likely violated given the anatomic characteristics of the cervix. Moreover, the stress measurement system and strain quantification algorithm are independent of ultrasound machines, which means that they can be interfaced with different machines with relatively minor software updates. This cross-platform feature allows these measurements to be adapted regardless of the ultrasound platform used, making the technology scalable clinically and commercially.

Future updates to improve the system include improving the precision of estimating Young's moduli in anatomic region-specific areas of cervical tissue, which could begin to map different geographic changes within the cervical anatomy over pregnancy. For example, Young's modulus specifically of the anterior cervical region, posterior cervical region, or area most proximal to the uterine cavity could be interrogated individually to ascertain global versus region-specific softening and association with obstetric conditions. Measurement from a single stress sensor is currently used to approximate the average stress along the probe axis. To further improve the accuracy, we may use multiple sensors and finite element mechanical modeling to estimate the stress distribution. Also, the current image-based strain quantification does not fully utilize the ultrasound system's resolution due to the loss of high-frequency components in image formation. Further study may perform strain quantification through RF signal (when available) directly to achieve higher accuracy in local strain quantification. Continued optimization of the stress sensor sensitivity, stress calibration system, ease of sensor application, and automatic image/signal processing are all steps that could be refined to make this technology more efficient and scalable in the future.

## V. CONCLUSION

The proposed system is accurate, robust, and safe in quantifying cervical tissue elasticity, and enables longitudinal measurements and comparisons between examiners. It will allow investigations documenting normal and abnormal cervical softening patterns in pregnancy and can be used in clinical populations to quantify risks for obstetric conditions associated with abnormal cervical physiology (preterm birth, post-term birth, cervical insufficiency, etc.). This technology has wide applicability to research endeavors and multiple potential clinical uses.

## REFERENCES

[1] H. A. Frey and M. A. Klebanoff, "The epidemiology, etiology, and costs of preterm birth," *Seminars Fetal Neonatal Med.*, vol. 21, no. 2, pp. 68–73, 2016.

[2] V. Berghella et al., "Cervical length screening for prevention of preterm birth in singleton pregnancy with threatened preterm labor: Systematic review and meta-analysis of randomized controlled trials using individual patient-level data," *Ultrasound Obstet. Gynecol.*, vol. 49, no. 3, pp. 322–329, 2017.

[3] R. B. Newman et al., "Preterm prediction study: Comparison of the cervical score and Bishop score for prediction of spontaneous preterm delivery," *Obstet. Gynecol.*, vol. 112, no. 3, pp. 508–515, Sep. 2008.

[4] R. M. Sigrist et al., "Ultrasound elastography: Review of techniques and clinical applications," *Theranostics*, vol. 7, no. 5, 2017, Art. no. 1303.

[5] A. Evans et al., "Quantitative shear wave ultrasound elastography: Initial experience in solid breast masses," *Breast Cancer Res.*, vol. 12, no. 6, 2010, Art. no. R104.

[6] J.-L. Gennisson et al., "Ultrasound elastography: Principles and techniques," *Diagn. Interventional Imag.*, vol. 94, no. 5, pp. 487–495, 2013.

[7] T. Shiina et al., "WFUMB guidelines and recommendations for clinical use of ultrasound elastography: Part 1: Basic principles and terminology," *Ultrasound Med. Biol.*, vol. 41, no. 5, pp. 1126–1147, 2015.

[8] G.-Y. Li and Y. Cao, "Mechanics of ultrasound elastography," *Proc. Math. Phys. Eng. Sci.*, vol. 473, no. 2199, Mar. 2017, Art. no. 20160841.

[9] A. Ozturk et al., "Principles of ultrasound elastography," *Abdominal Radiol.*, vol. 43, no. 4, pp. 773–785, Apr. 2018.

[10] T. Varghese, "Quasi-static ultrasound elastography," *Ultrasound Clin.*, vol. 4, no. 3, pp. 323–338, Jul. 2009.

[11] G. Treece et al., "Real-time quasi-static ultrasound elastography," *Interface Focus*, vol. 1, no. 4, pp. 540–552, Aug. 2011.

[12] K. M. Hiltawsky et al., "Freehand ultrasound elastography of breast lesions: Clinical results," *Ultrasound Med. Biol.*, vol. 27, no. 11, pp. 1461–1469, 2001.

[13] Q.-L. Zhu et al., "Real-time ultrasound elastography: Its potential role in assessment of breast lesions," *Ultrasound Med. Biol.*, vol. 34, no. 8, pp. 1232–1238, 2008.

[14] G. Salomon et al., "Evaluation of prostate cancer detection with ultrasound real-time elastography: A comparison with step section pathological analysis after radical prostatectomy," *Eur. Urol.*, vol. 54, no. 6, pp. 1354–1362, 2008.

[15] G. Ferraioli et al., "Performance of real-time strain elastography, transient elastography, and aspartate-to-platelet ratio index in the assessment of fibrosis in chronic hepatitis C," *Amer. J. Roentgenol.*, vol. 199, no. 1, pp. 19–25, 2012.

[16] M. Friedrich-Rust et al., "Evaluation of strain elastography for differentiation of thyroid nodules: Results of a prospective DEGUM multicenter study," *Ultraschall Medizin-Eur. J. Ultrasound*, vol. 37, no. 3, pp. 262–270, 2016.

[17] G. Ferraioli et al., "Liver ultrasound elastography: An update to the world federation for ultrasound in medicine and biology guidelines and recommendations," *Ultrasound Med. Biol.*, vol. 44, no. 12, pp. 2419–2440, Dec. 2018.

[18] S. H. Lee et al., "Added value of shear-wave elastography for evaluation of breast masses detected with screening US imaging," *Radiology*, vol. 273, no. 1, pp. 61–69, Oct. 2014.

[19] R. G. Barr and Z. Zhang, "Shear-wave elastography of the breast: Value of a quality measure and comparison with strain elastography," *Radiology*, vol. 275, no. 1, pp. 45–53, Apr. 2015.

[20] J. H. Youk, H. M. Gweon, and E. J. Son, "Shear-wave elastography in breast ultrasonography: The state of the art," *Ultrasonography*, vol. 36, no. 4, pp. 300–309, Oct. 2017.

[21] J.-M. Correas et al., "Prostate cancer: Diagnostic performance of real-time shear-wave elastography," *Radiology*, vol. 275, no. 1, pp. 280–289, Apr. 2015.

[22] J.-M. Correas et al., "Ultrasound elastography of the prostate: State of the art," *Diagn. Interventional Imag.*, vol. 94, no. 5, pp. 551–560, May 2013.

[23] G. Ferraioli et al., "Accuracy of real-time shear wave elastography for assessing liver fibrosis in chronic hepatitis C: A pilot study," *Hepatology*, vol. 56, no. 6, pp. 2125–2133, 2012.

[24] C. H. Suh et al., "Determination of normal hepatic elasticity by using real-time shear-wave elastography," *Radiology*, vol. 271, no. 3, pp. 895–900, Jun. 2014.

[25] J. H. Yoon et al., "Hepatic fibrosis: Prospective comparison of MR elastography and US shear-wave elastography for evaluation," *Radiology*, vol. 273, no. 3, pp. 772–782, Dec. 2014.

[26] V. Y. Leung et al., "Quantitative elastography of liver fibrosis and spleen stiffness in chronic hepatitis B carriers: Comparison of shear-wave elastography and transient elastography with liver biopsy correlation," *Radiology*, vol. 269, no. 3, pp. 910–918, 2013.

[27] A. E. Samir et al., "Shear-wave elastography for the estimation of liver fibrosis in chronic liver disease: Determining accuracy and ideal site for measurement," *Radiology*, vol. 274, no. 3, pp. 888–896, Mar. 2015.

[28] F. Sebag et al., "Shear wave elastography: A new ultrasound imaging mode for the differential diagnosis of benign and malignant thyroid nodules," *J. Clin. Endocrinol. Metab.*, vol. 95, no. 12, pp. 5281–5288, 2010.

[29] A. Y. Park et al., "Shear wave elastography of thyroid nodules for the prediction of malignancy in a large scale study," *Eur. J. Radiol.*, vol. 84, no. 3, pp. 407–412, Mar. 2015.

[30] C.-K. Zhao and H.-X. Xu, "Ultrasound elastography of the thyroid: Principles and current status," *Ultrasonography*, vol. 38, no. 2, pp. 106–124, Apr. 2019.

[31] L. C. Carlson et al., "Changes in shear wave speed pre- and post-induction of labor: A feasibility study: Shear wave speed in induction of labor," *Ultrasound Obstet. Gynecol.*, vol. 46, no. 1, pp. 93–98, Jul. 2015.

[32] L. C. Carlson et al., "Detection of changes in cervical softness using shear wave speed in early versus late pregnancy: An in vivo cross-sectional study," *Ultrasound Med. Biol.*, vol. 44, no. 3, pp. 515–521, Mar. 2018.

[33] L. C. Carlson et al., "Quantitative assessment of cervical softening during pregnancy with shear wave elasticity imaging: An in vivo longitudinal study," *Interface Focus*, vol. 9, no. 5, Oct. 2019, Art. no. 20190030.

[34] J. Lu et al., "The predictive value of cervical shear wave elastography in the outcome of labor induction," *Acta Obstetricia Gynecologica Scandinavica*, vol. 99, no. 1, pp. 59–68, Jan. 2020.

[35] S. Manchanda et al., "Quantitative sonoelastographic assessment of the normal uterus using shear wave elastography: An initial experience," *J. Ultrasound Med.*, vol. 38, no. 12, pp. 3183–3189, Dec. 2019.

[36] M. Muller et al., "Assessment of the cervix in pregnant women using shear wave elastography: A feasibility study," *Ultrasound Med. Biol.*, vol. 41, no. 11, pp. 2789–2797, Nov. 2015.

[37] S. O'Hara, M. Zelesco, and Z. Sun, "Shear wave elastography on the uterine cervix: Technical development for the transvaginal approach," *J. Ultrasound Med.*, vol. 38, no. 4, pp. 1049–1060, Apr. 2019.

[38] A. A. Gemici et al., "Shear wave elastography of the uterine cervix under different conditions with inter-operator agreement analysis," *Polish J. Radiol.*, vol. 85, pp. e245–e249, 2020.

[39] E. Hernandez-Andrade et al., "A soft cervix, categorized by shear-wave elastography, in women with short or with normal cervical length at 18–24 weeks is associated with a higher prevalence of spontaneous preterm delivery," *J. Perinatal Med.*, vol. 46, no. 5, pp. 489–501, Jul. 2018.

[40] H. Feltovich and T. J. Hall, "Quantitative imaging of the cervix: Setting the bar," *Ultrasound Obstet. Gynecol.*, vol. 41, no. 2, pp. 121–128, Feb. 2013.

[41] M. Issaoui et al., "Shear wave elastography safety in fetus: A quantitative health risk assessment," *Diagn. Interventional Imag.*, vol. 99, no. 9, pp. 519–524, Sep. 2018.

[42] J. B. Fowlkes, "Safety considerations for shear-wave elastography of the infant brain," *Pediatr. Radiol.*, vol. 50, no. 7, pp. 905–906, Jun. 2020.

[43] H. Latorre-Ossa et al., "Quantitative imaging of nonlinear shear modulus by combining static elastography and shear wave elastography," *IEEE Trans. Ultrason., Ferroelectr., Freq. Control*, vol. 59, no. 4, pp. 833–839, Apr. 2012.

[44] A. Fruscalzo et al., "Cervical elastography during pregnancy: A critical review of current approaches with a focus on controversies and limitations," *J. Med. Ultrason.*, vol. 43, no. 4, pp. 493–504, Oct. 2016.

[45] M. J. Stout et al., "A multidisciplinary prematurity research cohort study," *PLoS One*, vol. 17, no. 8, 2022, Art. no. e0272155.

[46] R. A. Fisher, "Statistical methods for research workers," in *Breakthroughs in Statistics*. Berlin, Germany: Springer, 1992, pp. 66–70.

[47] J. M. Bland and D. G. Altman, "Statistical methods for assessing agreement between two methods of clinical measurement," *Lancet*, vol. 1, no. 8476, pp. 307–310, Feb. 1986.

[48] M. Sestelo et al., "npregfast: An R package for nonparametric estimation and inference in life sciences," *J. Stat. Softw.*, vol. 82, no. 12, pp. 1–27, 2017.

[49] T. J. Hall et al., "Phantom materials for elastography," *IEEE Trans. Ultrason., Ferroelectr., Freq. Control*, vol. 44, no. 6, pp. 1355–1365, Nov. 1997.